Biomass Conversion and Biorefinery
https://doi.org/10.1007/s13399-023-04567-1

ORIGINAL ARTICLE

Investigation of physicochemical and biological properties of boron-doped biochar

Ayten Ateş[1] · Burçak Aydemir[1] · Kerim Emre Öksüz[2]

Received: 10 May 2023 / Revised: 22 June 2023 / Accepted: 29 June 2023

Abstract

Boron doping of biochar leads to the formation of activated oxygen species and pores and defects in the carbon structure Therefore, boron-containing biochar was prepared by treating boric acid (H_3BO_3) solutions in different concentrations of hazelnut shells before pyrolysis. DSC results showed that treatment of biomass with solutions containing a low concentration (0.1 wt. %) of H_3BO_3 increased the degradation of cellulose and hemicellulose, but also increased char formation. However, treatment with solutions containing 2% and 5% H_3BO_3 increased biochar oxidation with the formation of boron oxide (B_2O_3). The FT-IR and XPS results showed the presence of B–B, B–O, and B–O–B in the H_3BO_3 treatment, which is due to the formation of B_2O_3. The examination of the proliferation of L929 mouse fibroblast cells in response to different concentrations of boron-containing biochars using the MTT assay revealed that biochar treated with 2% H_3BO_3 promoted cell growth (100.32 ± 1.93). However, above this concentration, the formation of polycrystalline B_2O_3 species exhibited an inhibitory effect on cell proliferation (81.98 ± 1.26) in the samples of H_3BO_3-doped biochar with 5% concentration. The results of the in vitro hemolysis tests for undoped biochar and high boron-containing (% 5) biochar sample showed mild hemolytic activity, with percentages of 2.46 ± 0.02 and 3.08 ± 0.04, respectively, according to the reported standards. Antimicrobial studies have shown that *Candida albicans* (a yeast, ATCC 10231) is more sensitive to H_3BO_3 than *Staphylococcus aureus* (Gram-positive bacteria, ATCC 29213). Boron-containing biochar can be used in a variety of applications, including biosensing, drug delivery, biological scaffolds, and biological imaging, as well as an adsorbent in the removal of pollutants and a catalyst in oxidation and electrochemical reactions.

Keywords Boron doping · Biochar · Boric acid · Hemolytic properties · Antimicrobial activity · Pyrolysis

1 Introduction

Biochar has attractive properties, such as low cost, abundant sources, simple processing techniques, and a promising future as a carbon-based material for various purposes. However, the lack of sufficient active sites and active ingredients in pristine biochar limits its use. It has been reported that the surface chemical bonding and chemical environment are significantly improved by the addition of non-metallic elements (e.g., N, P, and S) to biochar [1–3]. However, heteroatoms can destroy the physical and chemical structure of biochar. For this purpose, the element boron (B), the neighbor of carbon (C) in the periodic table, offers great advantages as it easily forms covalent molecules between C and O atoms during charring, along with its green, safe, low price, and extreme similarity to carbon in atomic groups [4–6]. This changes the electron transfer rate in the structure, forming defects and active centers [7]. In fact, the oxygen species generated by boron addition can also modulate the electronic structure and chemical structure of carbon surface [8]. Zhang et. al discovered that lignin can be modified with boric acid to increase its mechanical and thermal stability [9]. Hung et al. reported that boric acid treatment resulted in a significant reduction of total polycyclic aromatic hydrocarbons (PAHs), 61% in pineapple leaves biochar [10] and 85% in lignin biochar [11], which have significant mutagenic and carcinogenic potential for human and environmental health. This is due to oxidation of PAH precursors by boric acid.

✉ Ayten Ateş
ates@cumhuriyet.edu.tr

[1] Department of Chemical Engineering, Faculty of Engineering, Sivas Cumhuriyet University, Sivas, Türkiye

[2] Department of Metallurgical and Materials Engineering, Faculty of Engineering, Sivas Cumhuriyet University, Sivas, Türkiye

Published online: 15 July 2023

Due to its high oxidation stability and advantageous graphitization of carbon, boric acid has also been described as a dopant for the preparation of carbonaceous materials and for improving their physicochemical properties [12] by creating active sites for adsorption and catalysis through the incorporation of electron-deficient Lewis acids (B atoms) into the carbon structure [13, 14]. According to Wang et al. (2004), the complexation of wood with boric acid can lead to the formation of hydrogen ions, which enhances the conversion of wood into biochar [15]. In addition, it was reported that the yield of biochar increased significantly when biomass was pyrolyzed in the presence of boric acid [16, 17]. Therefore, boric acid can be considered a good chemical activator for forming the pore structure of biochar, producing biochar with high yield and suppressing PAHs' formation for biocompatible material.

Biochar modified with boric acid is mainly used for electrochemical catalysis [18], or the degradation of pollutants [19–21]. Due to the physical and chemical properties of biochar activated with boric acid, the functional material can also be used in many other fields, including biosensing, drug release, biological scaffolds, and biological imaging. In the field of biosensing, biochar activated with boric acid can be employed as a sensing platform to detect and analyze biological substances or chemical markers. Its high surface area and porosity make it an ideal substrate for immobilizing biomolecules, enabling sensitive and selective detection of target analysts. Furthermore, biochar activated with boric acid can be utilized in drug release systems. Its porous structure allows for efficient loading and controlled release of pharmaceutical agents. By incorporating drugs into the biochar matrix, it is possible to design delivery systems that ensure sustained and targeted release, improving therapeutic outcomes and reducing side effects. Additionally, this functional material holds promise in the realm of biological scaffolds. Due to its biocompatibility and porous nature, biochar activated with boric acid can serve as a scaffold for tissue engineering and regenerative medicine. It provides a three-dimensional structure that supports cell adhesion, proliferation, and differentiation, facilitating the growth of new tissues and organs.

Its unique properties make it suitable for use as a contrast agent in imaging techniques such as magnetic resonance imaging (MRI) or computed tomography (CT). By enhancing the contrast between different tissues or structures, biochar activated with boric acid aids in visualizing and diagnosing various biological processes or abnormalities. Its versatility and potential for customization make it a valuable functional material in advancing research and applications in these domains compared to the traditional materials.

Based on the above findings, a detailed study was conducted to investigate the physicochemical and biological properties of hazelnut shell biochar treated with boric acid. To accomplish this, boron-doped biochar was prepared using various concentrations of boric acid solutions and thoroughly characterized.

Cytocompatibility, hemocompatibility, and antibacterial activity tests were performed against both Gram-positive *Staphylococcus aureus* and *Candida albicans* to enable the use of boric acid-activated biochar samples in many other fields, especially biotechnology.

2 Experimental studies

2.1 Preparation of raw materials

Hazelnut shells (HS) were used as raw material for the production of biochar. The HS was obtained from the hazelnuts harvested in the 2019 harvest season in Çavuşlar district of Ordu. HS was ground into powder in the mill. The ground HS biomass was passed through sieves with particle sizes of 355–250 µm. Boric acid (H_3BO_3) was purchased from Merck (Darmstadt, Germany) and used without purification.

2.2 Preparation of biochar and boron-doped biochar

First, 5 g of HS was placed in a crucible, sealed with a lid, and pyrolyzed in a muffle furnace at 500 ^{o}C with a heating rate of 10 °C/min for 1 h. After washing and drying, the sample was denoted as BC. For comparison with the biochar, the pyrolysis of HS treated with boric acid was carried out. For this purpose, 0.1, 2, and 5 wt. % H_3BO_3 solutions were prepared. For this purpose, 0.1, 2, and 5 g of H_3BO_3 were weighed and each amount was dissolved in 100 mL of distilled water. 9 mL of the H_3BO_3 solutions was treated with 3 g of HS (355–250 µm) and kept for 1 day. Then, the mixtures were placed in a crucible, sealed with a lid, and pyrolyzed under the same condition of BC. The samples prepared were designated as Bx-BC, where x indicates the weight percentage of H_3BO_3.

2.3 Characterization of samples

While the composition of the biochar was determined using an elemental analyzer (CHNS/O) and EDS, the boron content of the boron-doped biochar samples was determined using ICP-MS (Thermo Scientific, iCAP Q Series ICP-MS). The elemental composition (C, H, N, and S) of the HS and biochar samples was measured using an elemental analyzer (Thermo Scientific's Flash 2000/MAS 200R, USA) and the oxygen (O) content of the samples was determined using mass balance. The elemental composition of the boron-doped biochar samples was determined using an energy dispersive X-ray spectroscopy instrument (EDS, Oxford

Instruments Inca, X-Act/51-ADD0013) connected to the Tescan Mira3 XMU FESEM.

The surface area and pore size distribution (micro-mesopore structure) of the prepared biochar were determined using Quantachrome Autosorb1C analyzer (FL, USA). Nitrogen with a purity of 99.99% was used as the adsorption gas. The surface area, pore volume, and micropore volume were calculated using the multipoint Brunauer–Emmett–Teller (BET) techniques, t-plot, and DR (Dubinin-Radushkevic) techniques, respectively. Using the Barrett, Joyner, Halenda (BJH) approach based on the Kelvin equation, the distribution of pore sizes was determined. With $P/P^o = 0.99$, the total pore volume (V_T) was considered the adsorbed volume, with adsorption and desorption occurring simultaneously. All samples were analyzed using the same methods for comparison. The Autosorb 1C package program was used for the calculations.

FT-IR (Fourier transform infrared) analysis was applied to the samples to determine the functional groups of the biochar. Samples were analyzed using a BrukerAplha FT-IR instrument. For the analysis, each sample of 0.15 g KBr and 0.0015 g sample was weighed and prepared in tablet form and analyzed for their functional groups. Spectra were recorded in the wavelength range of 400–4000 cm^{-1}.

Field emission scanning electron microscopy (FESEM) analyses of particle size and distribution were visualized with the TescanMira3 XMU (Brno, Czech Republic) instrument using the SE detector with a 5-nm gold plating result. Energy-dispersive X-ray spectroscopy (EDS) for elements corresponding to each sample was determined by EDS analysis using TESCAN image processing software.

Differential scanning calorimeter (DSC) measurements of the raw material and a mixture of boric acid and biomass were performed under conditions of pyrolysis using the DSC-60 Plus/60A (Schimadzu Corporation, Japan) instrument.

X-Ray diffraction (XRD) analyses of the biochar samples were performed using a D/tex Ultra 250 detector and Cu-K_β radiation with a wavelength of $\lambda = 1.5$ Å at 40 kW 30 mA conditions ranging from 5 to 90 of 2θº.

Thermo Scientific K-Alpha has been used as the subject of X-ray photoelectron spectroscopy (XPS), using Al K X-rays as the excitation source.

2.4 In vitro cytocompatibility

ISO 10993–5 standard test method was used to evaluate the cytotoxicity of the biochar samples in vitro. A total of 4 different compositions of synthesized biochar samples in a 10-mm circular dish were sterilized at 120 °C and 2 bar for 20 min. Then, the biochar samples were placed in a 24-well plate and immersed in a cell culture medium for 12 h prior to the cell culture experiment. All experiments were carried out using an L929 mouse fibroblast cell line purchased from ATCC (USA, VA) and maintained in Dulbecco's Modified Eagle Medium (DMEM, Sigma-Aldrich, USA, MO) containing 1% (v/v) of pre-made penicillin (100 units/mL) and streptomycin solution (100 units/mL), and 10% (v/v) fetal bovine serum (FBS, HyClone, US, UT). Cells were grown at 37 °C in a humidified incubator containing 5% CO_2 and the culture medium was refreshed every 2 to 3 days. Cell viability was determined by the 3-(4,5-dimethylthiazol-2-yl)-2,5-diphenyltetrazolium bromide (MTT) assay. L929 mouse fibroblast cells were seeded in a 96-well plate with growth media, then treated with biochar samples and incubated for 24 h.

After incubation, MTT assays were conducted by adding 10 µL of MTT reagent to each well and incubating at 37 °C and 5% CO_2 for 2 h. Absorbance was measured spectrophotometrically using a Thermo Scientific Multiskan FC Microplate Photometer Reader (Thermo Scientific, U.S.A.) at a wavelength of 450 nm. Cell viability was determined by calculating the percentage of viability in the control sample, which was considered 100% [22, 23].

2.5 Hemolysis test

In vitro hemocompatibility studies of biochar samples were performed according to ISO 10993–5:1992 and Standard Practice for Assessment of Hemolytic Properties of Materials from the American Society for Testing and Materials (ASTM F756-00, 2000) [24, 25]. Three blood samples were collected from healthy sheep at a slaughterhouse and then stabilized with ethylenediaminetetraacetic acid (EDTA, 1.8 mg/mL). After centrifugation of the blood at 3000 rpm for 15 min, the plasma (supernatant) was removed. After centrifugation, 1 mL of red blood cells (RBCs) was rinsed 3 times with sterile PBS solution (pH 7.2 ± 0.2) and diluted 10 times with sterile $1 \times$PBS. Sterile biochar samples were placed in sterile polypropylene test tubes; then, 2 mL RBCs were added to the biochar samples and incubated at 37 °C for 2 h. During the incubation period, the test tubes were gently shaken for every 60 min. After incubation, the tubes were centrifuged at 3000 rpm for 5 min, and the supernatant solution was collected. Optical density values of the supernatants were then recorded at 541 nm using the SPECTROstar Nano (Germany) equipped with the ultra-fast UV/vis spectrometer from BMG LABTECH.

A positive control was set with 0.2 mL of RBCs and 0.8 mL of distilled water, whereas a negative control was set with PBS. The percentage of hemolysis was determined using the following formula:

$$\text{Hemolysis}(\%) = \frac{OD_S - OD_{NC}}{OD_{PC} - OD_{NC}} x100 \quad (1)$$

where OD_S is the absorbance value of the biochar sample tested, OD_{NC} is the absorbance value of the negative control,

and OD_{PC} is the absorbance value of the positive control. Experiments were performed three times to ensure consistency [26].

2.6 Antibacterial activity

The antibacterial properties of the biochar samples were evaluated according to the literature with some modifications [27, 28]. The antimicrobial assay of the biochar samples against *Staphylococcus aureus* (Gram positive bacteria, ATCC 29213) and *Candida albicans* (yeast, ATCC 10231) was performed using a viable cell count protocol. The selected colonies (*S. aureus*: prokaryotic microorganisms; *C. albicans:* eukaryotic microorganisms) were inoculated and cultured in Mueller–Hinton Broth (MHB) medium until mid-log growth phase. Indicator microorganisms were collected via centrifugation (at 1000 × g for 15 min) and subjected to three washes with a PBS solution. Subsequently, the concentrations of the microorganisms were adjusted to correspond to McFarland No. 0.5 (10^7 colony forming units (CFU) mL^{-1} for bacteria and yeasts). They were then diluted at 1/100 and 1000 µL of the bacterial/yeast suspension was mixed with 50 mg of biochar samples and incubated for 4 h at 37 °C (30 °C for *C. albicans*) under a relative humidity atmosphere (90% RH). Prior to testing, the entire biochar samples were washed with sterilized PBS and irradiated with UV light for 1 h for disinfection. For enumeration of microorganisms, a series of tenfold diluted suspensions were prepared in buffered peptone water and 1000 µL of each suspension dilution was spread onto MHA plates. Plates were then placed in an incubator set at 37 °C for 24 h for *S. aureus* and 30 °C for 48 h for *C. albicans* and CFUs (colony forming units) were counted on Mueller–Hinton agar plates at the end of the incubation period. All antibacterial tests were performed twice, and the average of the two replicates was used for calculations. Results were expressed as CFU/ml for each indicator microorganism.

2.7 Statistical analyses

Data collected were presented as means ± standard deviations of the mean SD based on at least six independent measurements. Data were subjected to statistical analysis using the one-way method ANOVA, followed by application of Dunnett's and Tukey's test methods. Significance was reached at $*p \leq 0.05$ using Origin Pro 9.0 software (OriginLab Co., Northampton, USA).

3 Results and discussion

3.1 Characterization of biochar samples

The hazelnut shell biomass consists of cellulose, hemicellulose, and lignin, and its elemental composition involves 47.8% C, 45.4% O, 0.3% N, and 6.5% H. The DSC result for pyrolysis of HS under inert atmosphere at 500 °C for 1 h is shown in Fig. 1. The endothermic peak occurring in the range of 80–130 °C is related to the removal of moisture in HS. A broad peak in the range of 180–290 °C associated with the moister peak is related to the decomposition of hemicellulose and the peak between 360 and 420 °C shows the decomposition of cellulose. At temperatures above 425 °C, decomposition of lignin begins and continues until 900 °C. The decomposition peaks are consistent with the results in [29, 30]: in the range of 220–315 °C for hemicellulose, 315–400 °C for cellulose, and 160–900 °C for lignin. The biochar produced under similar conditions contains 78.9% C, 17.4% O, 3.2% H, and 0.5% N. Comparison with the raw biochar material confirms the DSC results by increasing carbonization and decreasing oxygen and hydrogen content by dehydroxylation.

When HS was treated with a boric acid solution, the decomposition temperatures for HS and boric acid changed significantly, as shown in Fig. 1. The DSC curve of pure boric acid is shown in Fig. S1. The main peak of boric acid at 155 °C is related to the first dehydration of boric acid ($2H_3BO_3 \rightarrow 2HBO_2 + 2H_2O$) as reported in [31, 32]. The undissociated pair of peaks in the range 160–180 °C is the second dehydration peak of boric acid via $HBO_2 \rightarrow 1/4H_2B_4O_7 + 1/4H_2O$. The decomposition peaks between 180 and 360 °C are assigned to the decomposition of pyroboric acid into boron trioxide [33], $1/4H_2B_4O_7 \rightarrow 1/2B_2O_3 + 3/2H_2O$.

The assignments of the peaks are consistent with the results in the literature [34]. However, due to the heating rate as stated by Huber et al., there is a slight difference between the actual results and those that were published [34]. Boric acid treatment shifted the occurrence of peaks at

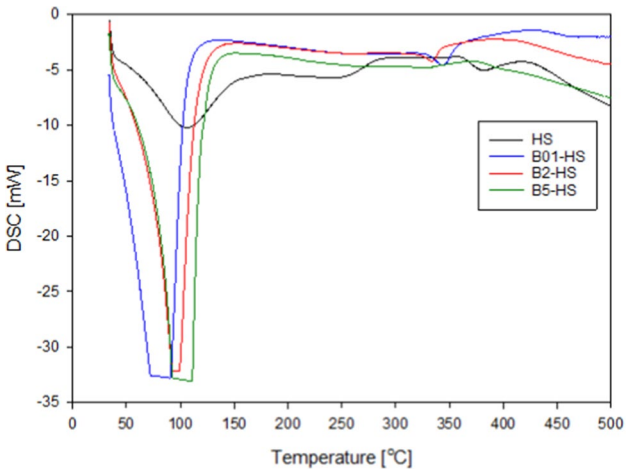

Fig. 1 DSC results of HS and boric acid-hazelnut shell mixture

about 375 °C in the pyrolysis of HS to lower temperatures: 340 °C for 0.1% boric acid and 320 °C for 2% boric acid. Comparison of the DSC results of HS and boric acid with those reported in [15, 35] indicates that the depolymerization of cellulose was particularly favored by the hydrogen ions generated during the complexation process between the hydroxyl and boric acid groups at low temperatures (about 100–300 °C).

The content of raw and pyrolyzed biochar is displayed in Table 1. The biochar's boron content increased with increasing boric acid concentration. Moreover, the highest carbon content (76.7%) was obtained with a 0.1% boron solution, since increasing boric acid concentration could lead to partial oxidation of the carbonaceous compounds. Boron cannot penetrate the structure of the biochar when the boric acid concentration is above 2% because it is removed when the biochar is washed after pyrolysis.

Figure 2 displays the XRD patterns of HS, biochar, and boric acid–activated biochar samples. The HS showed three peaks at 15.5°, 22.1°, and 35.0° of 2θº, which was due to amorphous cellulose [36]. Regardless of the presence of boric acid, the cellulosic peaks disappeared upon pyrolysis. The amorphous peak at about 25° of 2θº is related to the stable lignin content of the hazelnut shell. The intensity of amorphous carbon decreased via decomposition of unstable carbon with increasing boric acid concentration [11].

The FESEM images of raw and pyrolyzed samples are shown in Fig. 3. This can be clearly seen in the hazelnut shell samples, which have an inhomogeneous shape and surface area of the particles. When HS was pyrolyzed under the conventional conditions, the particles charred and formed a denser structure, and the surface became rougher. When the boric acid–treated HS was pyrolyzed, the surface morphology of the samples changed. In 0.1% of boric acid solution, the particles were distributed in layers on the surface, and in 2% of boric acid solution, the pores were open while the particles had a uniform shape. Treatment with a 5% boric acid solution of HS causes the formation of material consisting of thin layers and a smooth surface.

Figure 4 depicts N_2 adsorption–desorption isotherm and pore size distribution of the raw and pyrolyzed materials. According to the IUPAC classification, the isotherms of samples correspond to the type II [37], indicating that the samples are microporous and mesoporous, allowing the formation of multiple adsorption layers with increasing P/P^o. The surface properties of the samples were calculated from the isotherms of N_2 adsorption and desorption and are listed in Table 2. Conventional and boric acid–assisted pyrolysis of HS increased the specific surface area and total pore volume due to the formation of micropores and mesopores. Increasing the boric acid concentration leads to an increase in micropores and mesopores, as shown in Fig. 4. This can be explained by the catalytic effect of boric acid on the dehydration and depolymerization reactions of biochar. The highest surface area and pore volume were found to be 420.5 m^2/g and 0.26 cm^3/g, respectively, for B5-BC.

The FT-IR spectra of HS and biochar samples are shown in Fig. 5. The broad peak with a peak center of 3419 cm^{-1} in HS belongs to –OH groups [38], and its intensity decreases significantly as a result of dehydration reactions during pyrolysis at 500 °C. The peak pair in the range 2790–3000 cm^{-1} [38] is associated with aliphatic C–H groups and is removed from the structure by pyrolysis. The peak at about 2360 cm^{-1} that occurs during pyrolysis is the CO_2 peak [39].

The C = O stretching bond in ester groups and in nonconjugated ketones and carbonyls appears at 1738 cm^{-1} and disappears by pyrolysis [40]. The peak at 1618 cm^{-1} indicates the presence of COOH groups [41] and the center of the peak shifts to 1590 cm^{-1} upon pyrolysis. C=C at 1514 cm^{-1} is

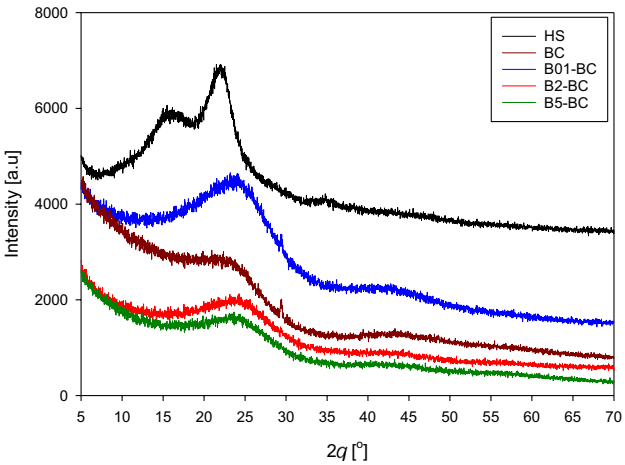

Fig. 2 XRD pattern of the HS, BC, boron containing biochar samples

Table 1 Composition of samples determined by ICP-MS and FE-SEM–EDS

Sample	B[a] %	B %	C %	O %	Mg %	Cl %	K %	Ca %	Al %
B01-BC	11.1	13.2	76.7	9.4	0.1	-	-	0.51	0.05
B2-BC	17.2	13.7	72.6	12.8	0.08	–	–	0.67	0.03
B5-BC	18.3	23.6	70.6	5.2	0.01	0.02	0.03	0.08	0.02

[a]Boron was determined by ICP-MS

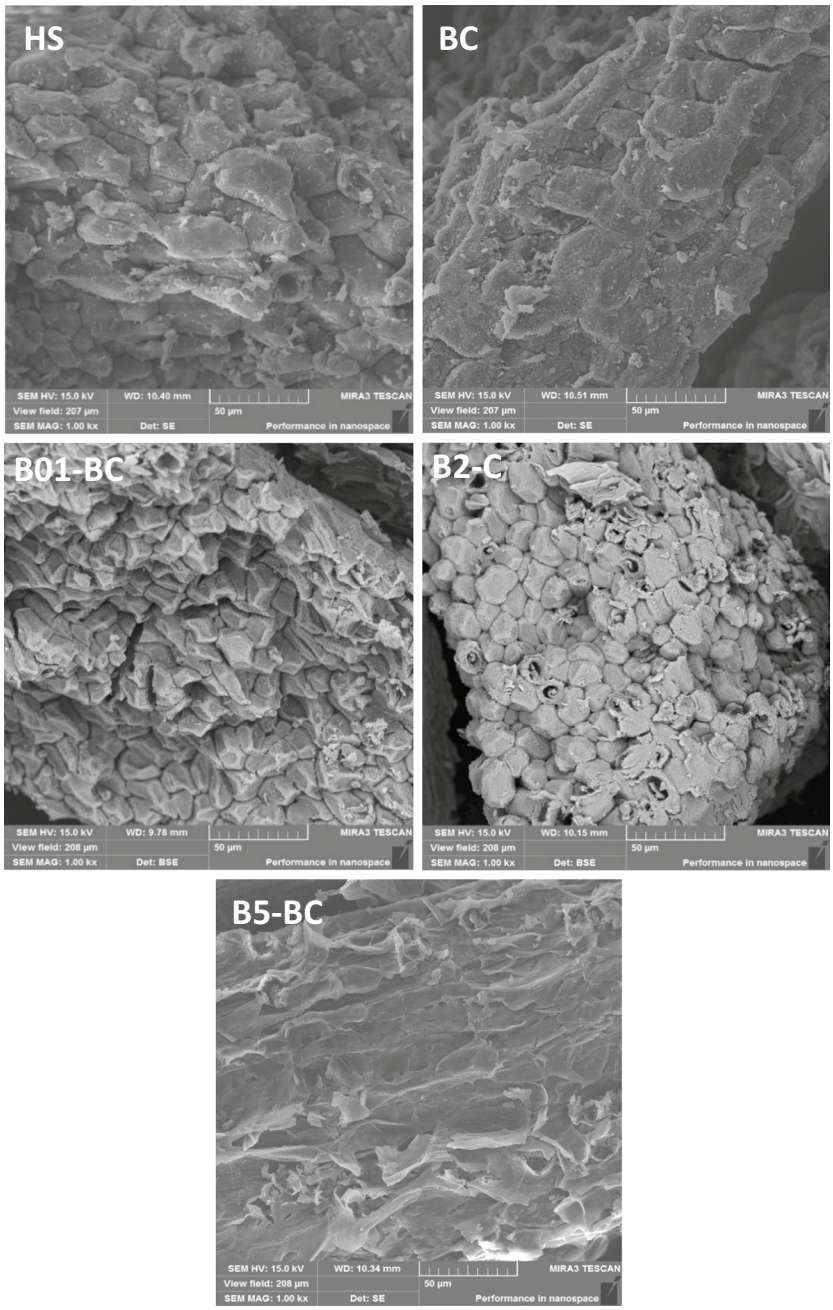

Fig. 3 FE-SEM photos of HS, BC, and boron-doped biochar samples

assigned to the stretching vibration of lignin [42]. Two peaks at 1458 and 1370 cm^{-1} indicate the presence of CH_2 groups in biopolymers [43]. The bands at 1258 and 1097 cm^{-1} are attributed to the νC–O of lignin [44], and are largely retained due to the stability of lignin during pyrolysis. The band at 1041 cm^{-1} can be assigned to the C–O–C of cellulose and mostly disappears due to pyrolysis, as seen in DSC results [45]. A large peak at about 575 cm^{-1} is found that can be attributed to O–C–O bending in esters [46] and its intensity decreases with pyrolysis due to decomposition of the esters. The peaks at 752, 820, and 872 cm^{-1}, which appear in HS with low intensity and are present in the biomass, indicate aromatic C–H bonds [47]. This can be attributed to the stability of the aromatic structure.

The FT-IR spectrum of the boron containing biochar samples shows the presence of functional groups with –CH, C = O, B–O, B–O–B, and –OH. The peak at 1703 cm^{-1} is due to the C = O stretching of ester [48], which increases slightly at a pyrolysis temperature of 500 °C. The band at about 1600 cm^{-1} is related to the C = O groups in the aromatic rings of lignin [49], showing that pyrolysis at 500 °C did not decompose this functional group. The peak at 1258 cm^{-1} shows the presence of acetyl groups in hemicellulose [50] and the weak peak at 1390 cm^{-1} is related to the B–O bond

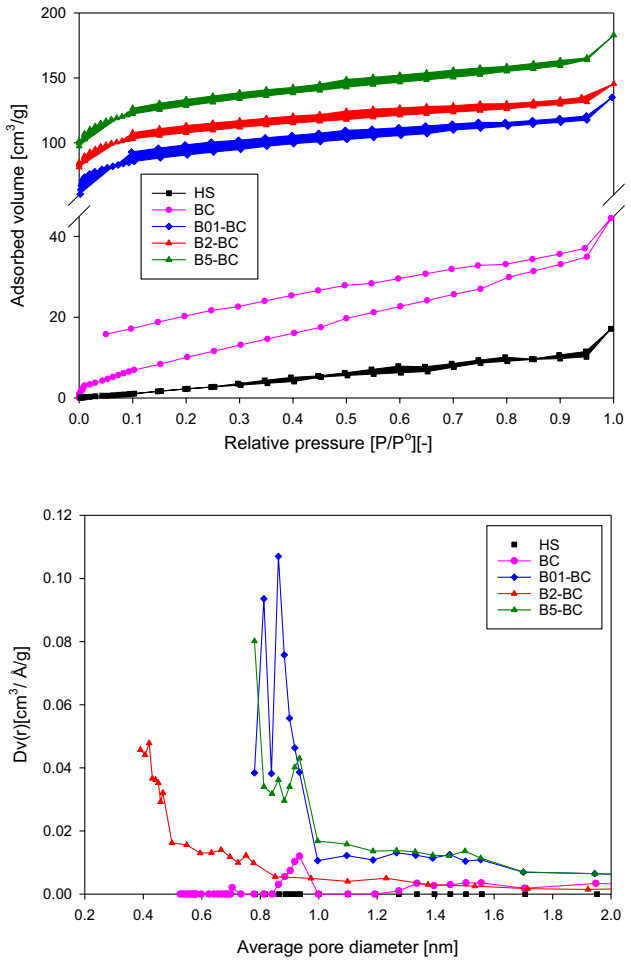

Fig. 4 N_2 adsorption–desorption isotherm and pore size distribution of samples

Table 2 Surface area and pore characteristics of raw and pyrolyzed biochar samples

Sample	S_{BET}[a] ($m^2\ g^{-1}$)	V_T[b] ($cm^3\ g^{-1}$)	V_M ($cm^3\ g^{-1}$)[c]	Dp[d] (nm)
HS	16.9	0.017	n.d	2.1
BC	47.4	0.057	n.d	2.4
B01-BC	307.5	0.18	0.11	1.2
B2-BC	350.7	0.20	0.14	1.1
B5-BC	420.5	0.26	0.16	1.2

[a]Multipoint BET surface area; [b]total pore volume calculated at $P/P^o = 0.99$; [c]micropore volume determined with DR method; [d]mean pore diameter determined by DR. *n.d*, not detected

[51], which increases slightly with increasing boron concentration as more B is introduced into the carbon structure. The bending vibrations of the B–O–B bonds in $[BO_4]$ units are responsible for the bands at about 752 cm^{-1} [52]. The absorption band at 895 cm^{-1} corresponds to the aromatic C–H vibrations [53], which are not affected by the boron concentration. The presence of the O–H stretching frequency of hydroxyl groups and the remaining adsorbed water were assumed to cause a broad band at 3370 cm^{-1} [54]. Moreover, the weak peaks at 2924 cm^{-1} are due to C–H stretching vibrations [55].

The XPS survey of the B5-BC is displayed in Fig. 6. The atomic content determined of the sample by XPS survey is 8.5% B, 54.5% C, 1.3% N, 19.4% O, and 4.6% P. Three peaks in C1s can be determined; C = C at 284.5 eV, C–N at 285.6 eV [56] and COO– and carboxyl group/ester groups at 289.1 eV [57]. Two oxygen peaks at 532.8 and 530.8 eV are assigned to C–O and –OH peaks [58]. The peaks matched for B1 s are identified as B-O at 191.6 eV and B_2O_3 at 194.1 eV [59] and B-B at 186. 8 eV [60]. XPS results show that the biochar prepared by treating boric acid solutions contains oxygenated carbonaceous compounds and B_2O_3.

3.2 Biocompatibility results

The MTT assay was used to investigate the effect of different biochar concentrations on the growth of L929 mouse fibroblast cells. The viability of cells in the biochar samples was expressed as a percentage of cell viability. Figure 7 shows the MTT assay protocol, photos of cell morphology of cells treated with different compositions of biochar samples, and the graph of cell viability (%) by MTT assay. From Fig. 7, it can be seen that cell proliferation was supported by all biochar groups as their cell viability values were above ~ 82%. In the experimental study conducted with different biochar samples, it was found that both materials were not cytotoxic.

When the cell viability of the biochar samples exceeds 70%, it indicates non-cytotoxicity according to the guidelines of the standard ISO 10993–5 [61, 62]. As shown in Fig. 7, a significant difference in cell activity was observed for the B2-BC group (100.32 ± 1.93), and it was found to support cell growth. However, cell viability was slightly reduced in the B5-BC group. Compared with the other biochar groups, the B5-BC media had a statistically significant lower value, suggesting that high boron dose may have an antiproliferative effect on cell proliferation. These reasons are attributed to the presence of a mixed polycrystalline boron oxide (B_2O_3) layer on the surfaces of the biochar samples. The biocompatibility results proved that the boron-doped biochar samples were highly biocompatible and non-toxic compared with the control group.

A significant concern related to the in vivo delivery of bioactive ions from biomaterials is whether the quantity of released ions falls within the therapeutic range to yield a beneficial impact [63]. Boron and its compounds have been found to promote cell proliferation and growth. The mechanism behind this phenomenon involves the dissolution products of boron compounds, particularly B_2O_3, which are formed during phase transformation. These dissolution products act as cell receptors, stimulating cell proliferation and

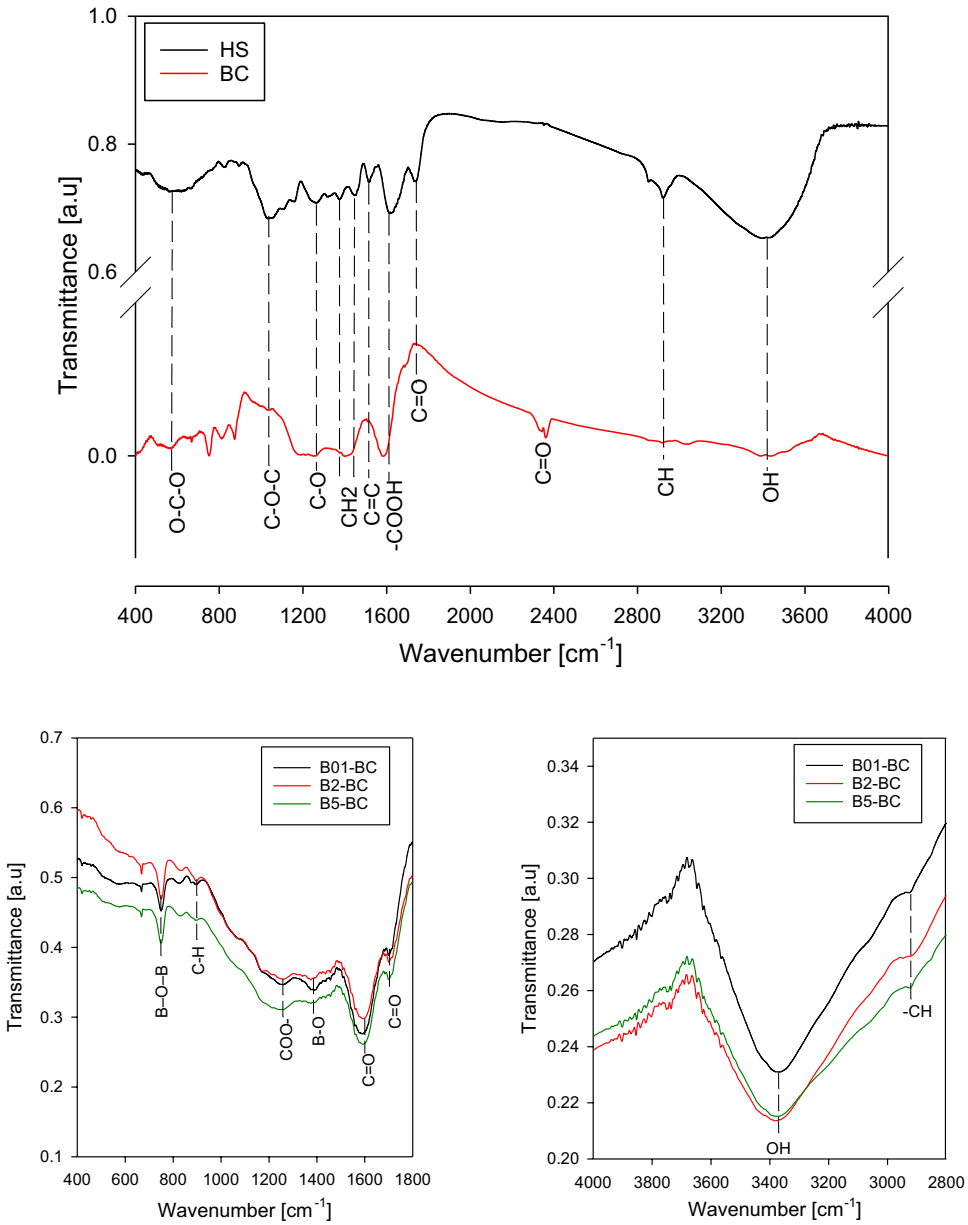

Fig. 5 FT-IR spectra of HS, BC, and boron containing biochar samples

growth [64, 65]. To understand why boron compounds have this effect, we need to delve into the interaction between cells and these compounds at a molecular level. When boron compounds such as B_2O_3 dissolve in aqueous solutions, they release borate ions ($B(OH)_4^-$) into the surrounding medium. Borate ions have a unique chemical structure that allows them to interact with certain biomolecules and cell receptors.

Borate ions can form reversible complexes with cis-diol groups present in various biomolecules, such as sugars, nucleic acids, and glycoproteins. This interaction is known as boronate ester formation. The formation of boronate esters with biomolecules can trigger specific signaling pathways within the cells, leading to enhanced cell proliferation and growth [66, 67]. The activation of a particular phenomenon exhibits a direct correlation with the concentrations of boron in the biochar samples, showcasing an upward trend as the concentration increases. However, it is noteworthy that once the boron concentration surpasses a certain threshold, a reversal occurs, leading to inhibition rather than further activation. While lower concentrations of boron facilitate the activation process, higher concentrations seem to exert an inhibitory effect, potentially indicating a saturation or overload of the system. Understanding the underlying mechanisms responsible for this dual behavior is essential to determine the optimal concentration range for achieving desired outcomes in various applications.

Research indicates that when boron compounds bind to cis-diol groups, they have the potential to traverse the

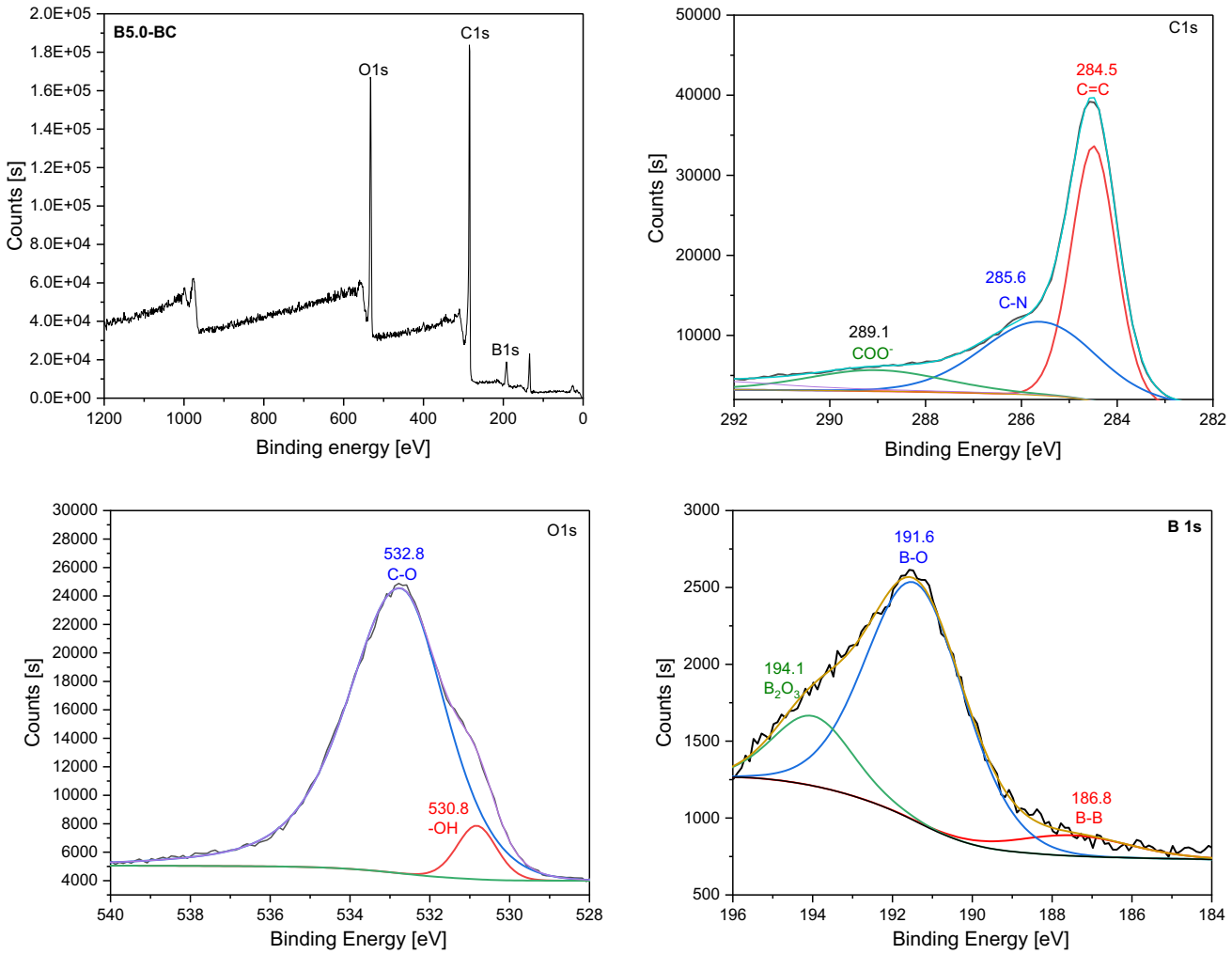

Fig. 6 XPS results of HS, BC, and boron containing biochar samples

cellular membrane and form associations with intracellular sugars [68]. Moreover, this binding interaction with sugars or oligosaccharides, which might display selectivity under specific conditions, could provide an explanation for boron's impact on RNA and protein synthesis. This is due to the occurrence of cis-diol groups in the ribose moieties of RNA [69]. Therefore, the binding of boron compounds to cis-diol groups could facilitate their entry into cells and potentially influence vital cellular processes, such as RNA and protein synthesis, leading to notable physiological effects.

Additionally, BC production through pyrolysis in the absence of oxygen is preferred. However, this method can result in the creation of highly toxic aromatic compounds known as PAHs [10]. PAHs are of great concern due to their high carcinogenic and mutagenic properties, which can negatively impact both human health and the environment. Recently, the introduction of heteroatom doping (such as N, B, O, P, and S) has emerged as a promising approach to impede the generation of toxic aromatic compounds, including PAHs, during BC formation [11, 21]. Furthermore, this doping method enhances biocompatibility. By incorporating heteroatoms, the surface properties of BC can be modified, resulting in enhanced interactions with biological entities such as cells, tissues, and biomolecules. This improved biocompatibility holds tremendous potential for various biomedical applications. It is crucial to emphasize that although boron and its compounds have exhibited promising effects in stimulating cell proliferation, there is still ongoing research aimed at unraveling the precise underlying mechanisms and determining the optimal concentrations for diverse tissue types. While the positive outcomes of boron's influence on cell growth have been observed, a comprehensive understanding of the molecular pathways and cellular interactions involved is necessary to fully harness its potential in the field of bioengineering. Consequently, further studies are imperative to elucidate the intricate workings of boron compounds and their specific effects on various tissues, enabling the development of targeted and effective strategies for utilizing boron in chemical and biomedical

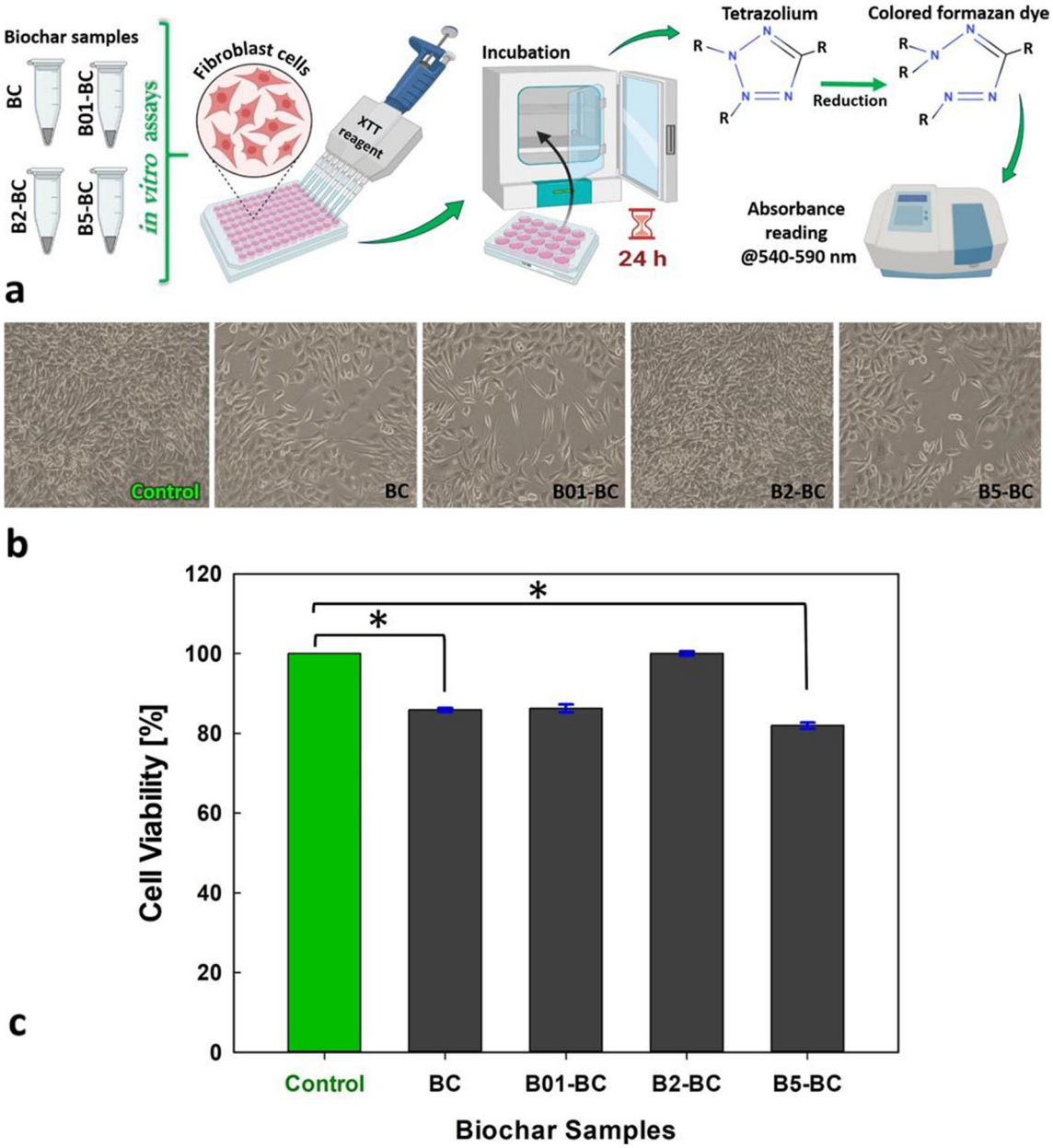

Fig. 7 (**a**) MTT assay protocol of biochar samples, (**b**) optical microscopy images and cell morphology of fibroblast cells treated with various compositions of biochar samples. Representative microscopic images (×20 magnification) of control groups before and after exposure to biochar samples for 24 h. The corresponding cell viability is plotted in (**c**), in which (*) denotes that a significant difference was observed ($p < 0.05$) when compared to the control group, and the error bar means the standard deviation (± SD)

engineering applications. By continuing to investigate these aspects, scientists can optimize the use of boron and its compounds, advancing the field and potentially unlocking novel therapeutic approaches for biologic effect.

3.3 Hemocompatibility results

To assess the hemocompatibility of the biochar samples, an in vitro hemolysis assay was performed. Figure 8 shows the schematic representation of in vitro hemolysis test steps and hemolysis ratio (%) results of the biochar samples using fresh blood samples. The macroscopic color of all four biochar sample groups and the positive control group (RBCs/dH_2O = ¼ mL) was examined after incubating for 2 h at 37 °C. All biochar groups were pale yellow, whereas the positive control group was bright red. The hemolysis ratio was % 2.46 ± 0.02, % 2.35 ± 0.06, %3.45 ± 0.18, and %3.08 ± 0.04 for the BC, B01-BC, B2-BC, and B5-BC biochar groups, respectively

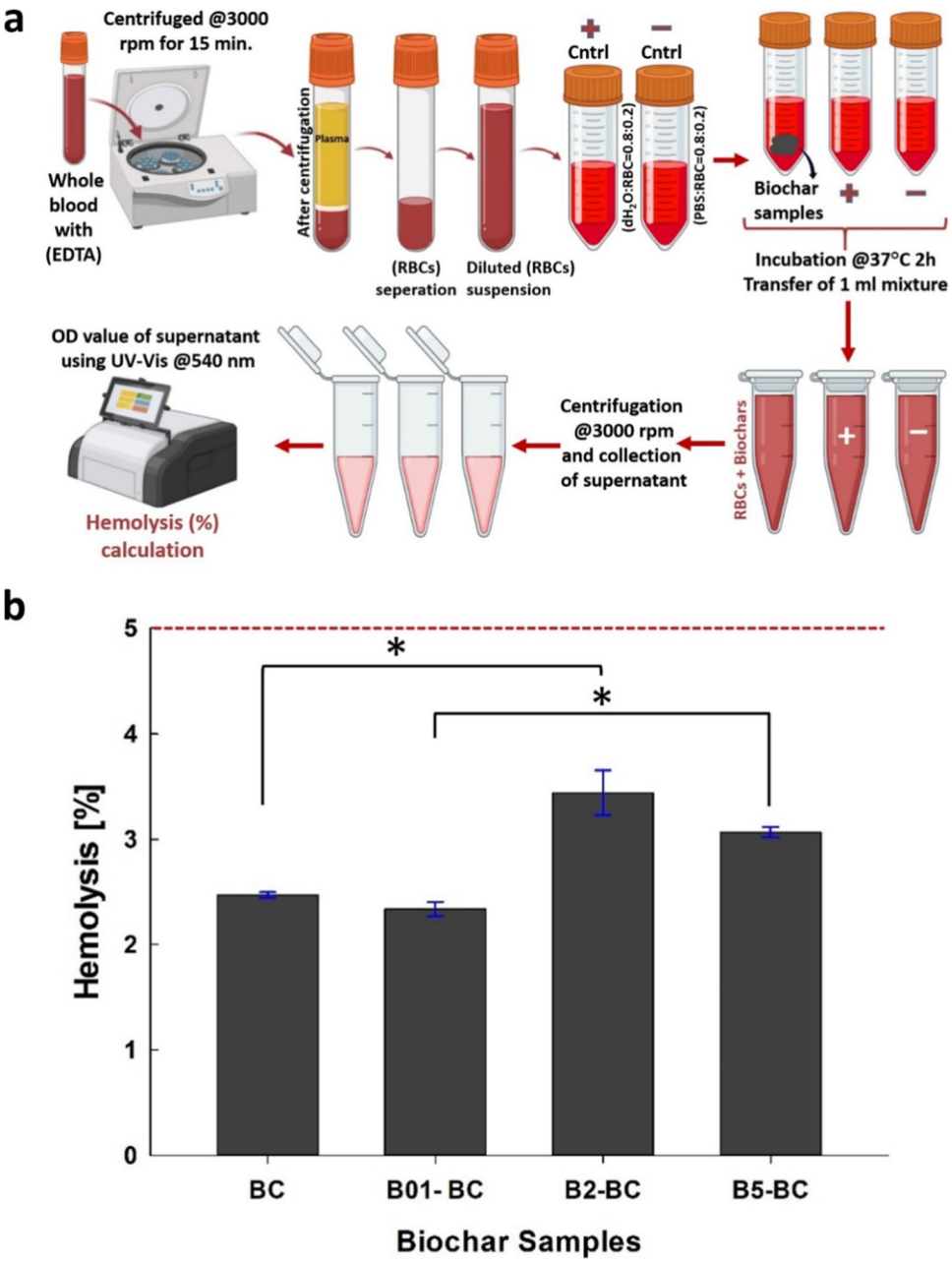

Fig. 8 (**a**) Schematic representation of in vitro hemolysis assay steps of the biochar samples. (**b**) Hemolysis ratio (%) of biochar samples. *Significant differences to all pairwise at $p < 0.05$*

(Fig. 8b). This indicates that hemolysis rates increase slightly with higher boron content.

It is well known that the external surface area of materials affects hemolysis by either modulating the number of red blood cells bound to nanoparticles or affecting the energy of cell membranes to encapsulate nanoparticles [70]. It is hypothesized that the B2-BC biochar group, which has the highest hemolysis ratio (%) value, is directly related to this phenomenon based on the experimental data obtained.

Furthermore, the external surface area of materials can also influence the adsorption and presentation of bioactive molecules or functional groups that may directly interact with red blood cells. This interaction can trigger biochemical responses, leading to changes in cell membrane integrity and subsequent hemolysis rates. Moreover, the morphology and surface topography of the materials can play a significant role in hemolysis. Materials with a larger external surface area often exhibit increased roughness or irregularities, providing more sites for potential interactions with red blood cells. These surface features can induce physical stress on the cell membrane, promoting hemolysis [71].

When considering the effect of boron content on hemolysis rates, it is crucial to account for the multifaceted nature of the materials external surface area, including its morphology, topography, and chemical composition [72]. These factors collectively contribute to the observed changes in

hemolysis, highlighting the complexity of the underlying mechanisms involved in the interaction between biochar samples and red blood cells.

In the determination and classification of the hemolytic activity of various materials to be used in healthcare, the American Society for Testing and Materials (ASTM) standards are generally accepted. The ASTM standards (ASTM F756-00) and ISO 10 993–51, 992 specify that a sample is considered non-hemolytic if the range of its hemolytic index is less than 2%, while a range between 2 and 5% is considered slightly hemolytic, and a range exceeding 5% is classified as hemolytic [73].

3.4 Antimicrobial activity

The antibacterial activity of the biochar samples against the growth of *S. aureus* and *C. albicans* was evaluated. A schematic illustration of the antibacterial assay steps, representative images of colony forming units for *S. aureus* and *C. albicans*, and the data of CFUs/mL^{-1} values of bacteria and yeast are summarized in Fig. 9. As can be seen in Fig. 9, it was found that the antibacterial activity against microorganism *S. aureus* showed no effect compared to the control group for all biochar samples with different amounts of boron oxides. Nevertheless, it is clear that the number of yeast colonies in the MHB plates of all biochar groups decreased significantly when the amount of boron oxides was increased to *C. albicans.* Previous studies have demonstrated the broad-spectrum of antimicrobial properties of boron compounds against various bacterial, fungal, and yeast species. In particular, studies have demonstrated the efficacy of boric acid and sodium borate against microorganisms such as *S. aureus*, *K. pneumoniae*, *C. albicans*, and *A. niger* [74, 75]. The inhibitory effect increases with increasing concentrations. Therefore, inhibition rates are strongly dependent on the level of boric oxide concentration. Based on these results, *Candida albicans* (a yeast, ATCC 10231) is more sensitive to boron oxides than *Staphylococcus aureus* (Gram positive bacteria, ATCC 29213).

Antimicrobial activity studies have shown that boron compounds can inhibit the growth of *C. albicans* by interfering with the cell wall and membrane of the yeast cells. The generation of oxygen-free radicals by boron oxide can harm cells and inhibit the growth of microorganisms. Boron compounds can also interfere with the production of enzymes and other proteins that are necessary for the growth and survival of the yeast cells. Boron compounds have the ability to stimulate the production of extracellular matrix glycoproteins and proteoglycans, which activate signaling and secretion pathways, even at lower concentrations. In addition, boron compounds can affect energy production in yeast cells, and all biochar samples with varying boron oxide content exhibited antibacterial properties compared to *S. aureus*, even at low concentrations. These results demonstrate that biochar samples doped with boron inhibit mycelial growth and the growth of *Candida albicans* yeasts [76, 77].

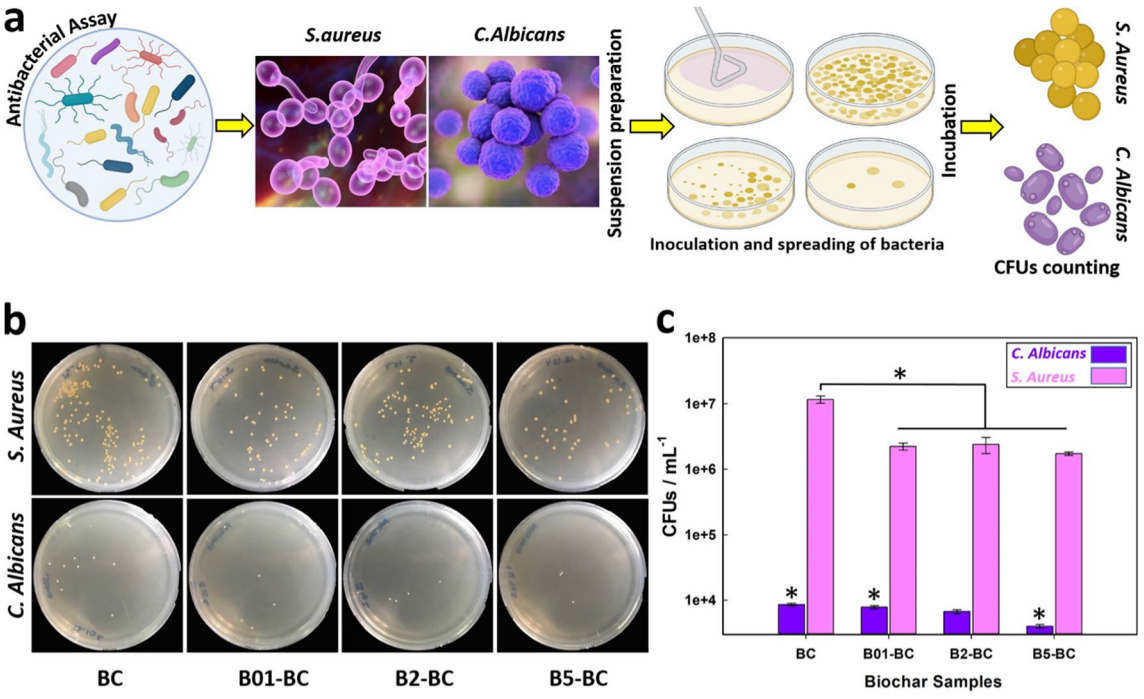

Fig. 9 (**a**) A schematic illustration of the antibacterial assay. (**b**) Optical images of survival bacterial colonies on MHA plates after contacting with biochar samples. (**c**) Antibacterial properties of the biochar samples against the *S. aureus* and *C. Albicans* (* indicates results that are significantly different from the result of the BC group ($p < 0.05$*))

4 Conclusions

Biochar samples containing boron were successfully prepared by pyrolysis after treatment of hazelnut hell with boric acid solutions. Boric acid treatment increases the charring of cellulose, hemicellulose, and lignin. All boron-doped biochar samples contain B–O, B–B, B–O–B, –OH, C–H, C = O, and COO– functional groups. Increasing the boric acid concentration increases the specific surface area and pore formation. Cytotoxicity evaluation shows that the boron-containing material is highly biocompatible and non-toxic. According to in vitro hemolysis tests, biochar and boron-containing biochar materials have low hemolytic activity. Based on the in vitro antibacterial activity of all samples, *Candida albicans* yeasts were significantly inhibited by increasing the boron content of biochar. The results suggest that boron-containing biochar possesses unique biological properties that make it a suitable option for use as a biomaterial in biomedical engineering. For this purpose, future works can address the following key aspects:

- Future research can focus on understanding the influence of different biochar production methods on boron toxicity. Exploring variations in pyrolysis temperature, duration, and feedstock composition can help optimize the manufacturing process to boron doped biochar samples.
- Evaluating the leaching potential of boron from biochar in diverse environmental conditions is crucial. Investigating factors such as environment pH, moisture levels, and organic matter content can enhance our understanding of boron mobility and its availability to other organisms.
- Detailed studies on the biochemical damages caused by boron-containing biochar are essential to assess its toxicity. Future research should explore the impact of biochar on growth, development, reproduction, and overall ecosystem health in various organisms. Investigating the cellular and molecular mechanisms of boron toxicity can provide valuable insights.

Supplementary Information The online version contains supplementary material available at https://doi.org/10.1007/s13399-023-04567-1.

Author contribution Ayten Ateş: conceptualization; investigation; methodology; writing original draft, review, and editing; supervision; funding acquisition. Burçak Aydemir: formal analysis, investigation, data curation. Kerim Emre Öksüz: formal analysis, methodology, writing original draft, review and editing.

Funding Project M-795 of Sivas Cumhuriyet University- Scientific Research (CUBAP) fund provided funding for this work. Authors thank for XPS analysis to TENMAK (Turkish Energy, Nuclear and Mineral Research Agency).

Data availability Not applicable.

Declarations

Ethical approval Not applicable.

Competing interests The authors declare no competing interests.

References

1. An N, Zhao M, Zheng X et al (2022) Synergistic oxytetracycline adsorption and peroxydisulfate-driven oxidation on nitrogen and sulfur co-doped porous carbon spheres. J Hazard Mater 424:127444. https://doi.org/10.1016/j.jhazmat.2021.127444
2. Wang W, Chen M (2022) Catalytic degradation of sulfamethoxazole by peroxymonosulfate activation system composed of nitrogen-doped biochar from pomelo peel: important roles of defects and nitrogen, and detoxification of intermediates. J Colloid Interface Sci 613:57–70. https://doi.org/10.1016/j.jcis.2022.01.006
3. Zheng R, Lin Q, Meng L et al (2022) Flexible phosphorus-doped activated carbon fiber paper in-situ loading of CuO for degradation of phenol. Sep Purif Technol 298:121619. https://doi.org/10.1016/j.seppur.2022.121619
4. Qu Z, Sun F, Gao J, Zhao G (2022) Activity origin of boron doped carbon cluster for thermal catalytic oxidation: coupling effects of dopants and edges. J Colloid Interface Sci 613:47–56. https://doi.org/10.1016/j.jcis.2022.01.017
5. Sawant SV, Patwardhan AW, Joshi JB, Dasgupta K (2022) Boron doped carbon nanotubes: synthesis, characterization and emerging applications–a review. Chem Eng J 427:131616. https://doi.org/10.1016/j.cej.2021.131616
6. Zhan H, Zhou Q, Li M et al (2022) Photocatalytic O2 activation and reactive oxygen species evolution by surface BN bond for organic pollutants degradation. Appl Catal B Environ 310:121329. https://doi.org/10.1016/j.apcatb.2022.121329
7. Duan X, O'Donnell K, Sun H et al (2015) Sulfur and nitrogen co-doped graphene for metal-free catalytic oxidation reactions. Small 11:3036–3044. https://doi.org/10.1002/smll.201403715
8. Lin Z, Wang X (2013) Nanostructure engineering and doping of conjugated carbon nitride semiconductors for hydrogen photosynthesis. Angew Chemie 125:1779–1782. https://doi.org/10.1002/ange.201209017
9. Zhang J, Koubaa A, Xing D et al (2020) Improving lignocellulose thermal stability by chemical modification with boric acid for incorporating into polyamide. Mater Des 191:108589. https://doi.org/10.1016/j.matdes.2020.108589
10. Hung C-M, Cheng J-W, Chen C-W et al (2023) Pyrolysis processes affecting polycyclic aromatic hydrocarbon profile of pineapple leaf biochar exemplified by atmosphere/temperature and heteroatom doping. Bioresour Technol 379:129047. https://doi.org/10.1016/j.biortech.2023.129047
11. Hung C-M, Chen C-W, Huang C-P et al (2022) Suppression of polycyclic aromatic hydrocarbon formation during pyrolytic production of lignin-based biochar via nitrogen and boron co-doping. Bioresour Technol 355:127246. https://doi.org/10.1016/j.biortech.2022.127246
12. Xin W, Song Y, Peng J et al (2017) Synthesis of biomass-derived mesoporous carbon with super adsorption performance by an aqueous cooperative assemble route. ACS Sustain Chem Eng 5:2312–2319. https://doi.org/10.1021/acssuschemeng.6b02637
13. Tian Z, Zhang Q, Thomsen L et al (2022) Constructing interfacial boron-nitrogen moieties in turbostratic carbon for electrochemical hydrogen peroxide production. Angew Chemie 134:e202206915. https://doi.org/10.1002/ange.202206915
14. Zhang J, Geng W, Shi L et al (2022) One–pot synthesis of boron and nitrogen co–doped nanocarbons for efficient catalytic

reduction of nitrophenols. Chem Eng J 439:135733. https://doi.org/10.1016/j.cej.2022.135733
15. Wang Q, Li J, Winandy JE (2004) Chemical mechanism of fire retardance of boric acid on wood. Wood Sci Technol 38:375–389. https://doi.org/10.1007/s00226-004-0246-4
16. Cheng X, Wang B (2017) Yield, composition, and property of biochar obtained from the two-step pyrolysis of rice husk impregnated with boric acid. Energies 10:1814. https://doi.org/10.3390/en10111814
17. Zhang J, Koubaa A, Xing D et al (2020) Conversion of lignocellulose into biochar and furfural through boron complexation and esterification reactions. Bioresour Technol 312:123586. https://doi.org/10.1016/j.biortech.2020.123586
18. Zhang F, Miao J, Liu W et al (2019) Heteroatom embedded graphene-like structure anchored on porous biochar as efficient metal-free catalyst for ORR. Int J Hydrogen Energy 44:30986–30998. https://doi.org/10.1016/J.IJHYDENE.2019.09.239
19. Liu B, Guo W, Wang H et al (2020) B-doped graphitic porous biochar with enhanced surface affinity and electron transfer for efficient peroxydisulfate activation. Chem Eng J 396:125119. https://doi.org/10.1016/j.cej.2020.125119
20. Hung C-M, Chen C-W, Huang C-P, Dong C-D (2022) Metal-free single heteroatom (N, O, and B)-doped coconut-shell biochar for enhancing the degradation of sulfathiazole antibiotics by peroxymonosulfate and its effects on bacterial community dynamics. Environ Pollut 311:119984. https://doi.org/10.1016/j.envpol.2022.119984
21. Hung C-M, Chen C-W, Huang C-P, Dong C-D (2023) Nitrogen and boron co-doped lignin biochar for enhancing calcium peroxide activation toward organic micropollutants decontamination in waste activated sludge and related microbial structure dynamics. Bioresour Technol 372:128673. https://doi.org/10.1016/j.biortech.2023.128673
22. Sigmund G, Huber D, Bucheli TD et al (2017) Cytotoxicity of biochar: a workplace safety concern? Environ Sci Technol Lett 4:362–366. https://doi.org/10.1021/acs.estlett.7b00267
23. Öksüz KE, Özkaya NK, İnan ZDŞ, Özer A (2021) Novel natural spider silk embedded electrospun nanofiber mats for wound healing. Mater Today Commun 26:101942. https://doi.org/10.1016/j.mtcomm.2020.101942
24. Alexandre N, Ribeiro J, Gärtner A et al (2014) Biocompatibility and hemocompatibility of polyvinyl alcohol hydrogel used for vascular grafting—in vitro and in vivo studies. J Biomed Mater Res Part A 102:4262–4275. https://doi.org/10.1002/jbm.a.35098
25. Wang C, Wang S, Li K et al (2014) Preparation of laponite bioceramics for potential bone tissue engineering applications. PLoS ONE 9:e99585. https://doi.org/10.1371/journal.pone.0099585
26. Ma Z, Bai J, Wang Y, Jiang X (2014) Impact of shape and pore size of mesoporous silica nanoparticles on serum protein adsorption and RBCs hemolysis. ACS Appl Mater Interfaces 6:2431–2438. https://doi.org/10.1021/am404860q
27. Gao L, Chen J, Feng W et al (2020) A multifunctional shape-adaptive and biodegradable hydrogel with hemorrhage control and broad-spectrum antimicrobial activity for wound healing. Biomater Sci 8:6930–6945. https://doi.org/10.1039/D0BM00800A
28. Singh S, Bhushan S, Das A et al (2023) Surgical cotton microfibers loaded with nanoceria: a new platform for bone tissue engineering. Ceram Int 49:1114–1127. https://doi.org/10.1016/j.ceramint.2022.09.087
29. Cao X, Zhong L, Peng X et al (2014) Comparative study of the pyrolysis of lignocellulose and its major components: characterization and overall distribution of their biochars and volatiles. Bioresour Technol 155:21–27. https://doi.org/10.1016/J.BIORTECH.2013.12.006
30. Yang H, Yan R, Chen H et al (2007) Characteristics of hemicellulose, cellulose and lignin pyrolysis. Fuel 86:1781–1788. https://doi.org/10.1016/j.fuel.2006.12.013
31. Grigorovskaya VA, Shashkin DP, Zapadinskii BI (2009) Low-temperature transformations of orthoboric acid. Russ J Phys Chem B 3:656–660. https://doi.org/10.1134/S199079310904023X
32. Sevim F, Demir F, Bilen M, Okur H (2006) Kinetic analysis of thermal decomposition of boric acid from thermogravimetric data. Korean J Chem Eng 23:736–740. https://doi.org/10.1007/BF02705920
33. Rotaru A (2017) Thermal and kinetic study of hexagonal boric acid versus triclinic boric acid in air flow. J Therm Anal Calorim 127:755–763. https://doi.org/10.1007/s10973-016-5583-7
34. Huber C, Jahromy SS, Birkelbach F et al (2020) The multistep decomposition of boric acid. Energy Sci Eng 8:1650–1666. https://doi.org/10.1002/ese3.622
35. Zhang J, Koubaa A, Xing D et al (2020) Conversion of lignocellulose into biochar and furfural through boron complexation and esterification reactions. Bioresour Technol 312:123586. https://doi.org/10.1016/J.BIORTECH.2020.123586
36. Ahn Y, Hu DH, Hong JH et al (2012) Effect of co-solvent on the spinnability and properties of electrospun cellulose nanofiber. Carbohydr Polym 89:340–345. https://doi.org/10.1016/J.CARBPOL.2012.03.006
37. Thommes M, Kaneko K, Neimark AV et al (2015) Physisorption of gases, with special reference to the evaluation of surface area and pore size distribution (IUPAC Technical Report). Pure Appl Chem 87:1051–1069. https://doi.org/10.1515/pac-2014-1117
38. Watanabe H, Shimomura K, Okazaki K (2013) Effect of high CO2 concentration on char formation through mineral reaction during biomass pyrolysis. Proc Combust Inst 34:2339–2345. https://doi.org/10.1016/J.PROCI.2012.07.048
39. Parshetti GK, Hoekman SK, Balasubramanian R (2013) Chemical, structural and combustion characteristics of carbonaceous products obtained by hydrothermal carbonization of palm empty fruit bunches. Bioresour Technol 135:683–689. https://doi.org/10.1016/j.biortech.2012.09.042
40. Schwanninger M, Rodrigues JC, Pereira H, Hinterstoisser B (2004) Effects of short-time vibratory ball milling on the shape of FT-IR spectra of wood and cellulose. Vib Spectrosc 36:23–40. https://doi.org/10.1016/J.VIBSPEC.2004.02.003
41. Mayakaduwa SS, Vithanage M, Karunarathna A et al (2016) Interface interactions between insecticide carbofuran and tea waste biochars produced at different pyrolysis temperatures. Chem Speciat Bioavailab 28:110–118. https://doi.org/10.1080/09542299.2016.1198928
42 Chen Z, Chen B, Chiou CT (2012) Fast and slow rates of naphthalene sorption to biochars produced at different temperatures. Environ Sci Technol 46:11104–11111. https://doi.org/10.1021/es302345e
43 Chen B, Johnson EJ, Chefetz B et al (2005) Sorption of polar and nonpolar aromatic organic contaminants by plant cuticular materials: role of polarity and accessibility. Environ Sci Technol 39:6138–6146. https://doi.org/10.1021/es050622q
44. Ocampo-Perez R, Padilla-Ortega E, Medellin-Castillo NA et al (2019) Synthesis of biochar from chili seeds and its application to remove ibuprofen from water. Equilibrium and 3D modeling. Sci Total Environ 655:1397–1408. https://doi.org/10.1016/J.SCITOTENV.2018.11.283
45. Xiao X, Chen B, Zhu L (2014) Transformation, morphology, and dissolution of silicon and carbon in rice straw-derived biochars under different pyrolytic temperatures. Environ Sci & Technol 48:3411–3419. https://doi.org/10.1021/es405676h
46. Asadinezhad A, Novák I, Lehocký M et al (2010) Polysaccharides coatings on medical-grade PVC: a probe into surface characteristics and the extent of bacterial adhesion. Molecules 15:1007–1027. https://doi.org/10.3390/molecules15021007
47. Usevičiūtė L, Baltrėnaitė-gedienė E, Feizienė D (2022) The combined effect of biochar and mineral fertilizer on triticale yield, soil properties under different tillage systems. Plants 11. https://doi.org/10.3390/plants11010111

48. Chen B, Zhou D, Zhu L (2008) Transitional adsorption and partition of nonpolar and polar aromatic contaminants by biochars of pine needles with different pyrolytic temperatures. Environ Sci Technol 42:5137–5143. https://doi.org/10.1021/es8002684
49. Fontana IB, Peterson M, Cechinel MAP (2018) Application of brewing waste as biosorbent for the removal of metallic ions present in groundwater and surface waters from coal regions. J Environ Chem Eng 6:660–670. https://doi.org/10.1016/J.JECE.2018.01.005
50. Kumar A, Gupta V, Gaikwad KK (2021) Microfibrillated cellulose from pine cone: extraction, properties, and characterization. Biomass Convers Biorefinery. https://doi.org/10.1007/s13399-021-01794-2
51. Chen X, Duan X, Da OhW et al (2019) Insights into nitrogen and boron-co-doped graphene toward high-performance peroxymonosulfate activation: maneuverable N-B bonding configurations and oxidation pathways. Appl Catal B Environ 253:419–432. https://doi.org/10.1016/J.APCATB.2019.04.018
52. Wang F, Wang Y, Chen J et al (2021) Effect of cerium oxide on phase composition, structure, thermal stability and aqueous durability of sodium-iron-boron-phosphate based glasses. J Nucl Mater 556:153199. https://doi.org/10.1016/J.JNUCMAT.2021.153199
53. Wang J, Zhang P, Peng J et al (2023) Sulfur and nitrogen co-doped magnetic biochar coupled with hydroxylamine for high-efficiency of persulfate activation and mechanism study. Environ Res 216:114745. https://doi.org/10.1016/J.ENVRES.2022.114745
54. Suwattanamala A, Bandis N, Tedsree K, Issro C (2017) Synthesis, characterization and adsorption properties of Fe3O4 /MWCNT magnetic nanocomposites. Mater Today Proc 4:6567–6575. https://doi.org/10.1016/J.MATPR.2017.06.169
55. Ahmed MB, Zhou JL, Ngo HH et al (2016) Progress in the preparation and application of modified biochar for improved contaminant removal from water and wastewater. Bioresour Technol 214:836–851. https://doi.org/10.1016/J.BIORTECH.2016.05.057
56. Jia H, Sun J, Xie X et al (2019) Cicada slough-derived heteroatom incorporated porous carbon for supercapacitor: ultra-high gravimetric capacitance. Carbon N Y 143:309–317. https://doi.org/10.1016/j.carbon.2018.11.011
57. Liu N, Charrua AB, Weng CH et al (2015) Characterization of biochars derived from agriculture wastes and their adsorptive removal of atrazine from aqueous solution: a comparative study. Bioresour Technol 198:55–62. https://doi.org/10.1016/J.BIORTECH.2015.08.129
58. Le Y, Guan Y, Ma X, Zhang W (2023) Preparation and boron removal performance of glycidol modified PANI nanorods: An optimization study based on response surface methodology. Polymers 15(2):459. https://doi.org/10.3390/polym15020459
59. Zhao W, Ma W, Chen C et al (2004) Efficient degradation of toxic organic pollutants with Ni2O3/TiO2-x B x under visible irradiation. J Am Chem Soc 126:4782–4783. https://doi.org/10.1021/ja0396753
60. Liu G, Yin LC, Niu P et al (2013) Visible-light-responsive β-Rhombohedral boron photocatalysts. Angew Chemie - Int Ed 52:6242–6245. https://doi.org/10.1002/anie.201302238
61. BS EN ISO, British Standards (2009) Biological evaluation of medical devices. https://doi.org/10.3403/BSENISO10993
62. Pettinelli N, Rodriguez-Llamazares S, Bouza R et al (2020) Carrageenan-based physically crosslinked injectable hydrogel for wound healing and tissue repairing applications. Int J Pharm 589:119828. https://doi.org/10.1016/j.ijpharm.2020.119828
63. Hoppe A, Mouriño V, Boccaccini AR (2013) Therapeutic inorganic ions in bioactive glasses to enhance bone formation and beyond. Biomater Sci 1:254–256. https://doi.org/10.1039/c2bm00116k
64. Nzietchueng RM, Dousset B, Franck P et al (2002) Mechanisms implicated in the effects of boron on wound healing. J Trace Elem Med Biol 16:239–244. https://doi.org/10.1016/S0946-672X(02)80051-7
65. Demirci S, Doğan A, Aydın S et al (2016) Boron promotes streptozotocin-induced diabetic wound healing: roles in cell proliferation and migration, growth factor expression, and inflammation. Mol Cell Biochem 417:119–133. https://doi.org/10.1007/s11010-016-2719-9
66. Wu C, Chang J (2014) Multifunctional mesoporous bioactive glasses for effective delivery of therapeutic ions and drug/growth factors. J Control Release 193:282–295. https://doi.org/10.1016/j.jconrel.2014.04.026
67. Durand LAH, Vargas GE, Romero NM et al (2015) Angiogenic effects of ionic dissolution products released from a boron-doped 45S5 bioactive glass. J Mater Chem B 3:1142–1148. https://doi.org/10.1039/c4tb01840k
68. Penn SG, Hu H, Brown PH, Lebrilla CB (1997) Direct analysis of sugar alcohol borate complexes in plant extracts by matrix-assisted laser desorption/ionization Fourier transform mass spectrometry. Anal Chem 69:2471–2477. https://doi.org/10.1021/ac970101o
69. Nagai Y, Kobayashi K, Toi H, Aoyama Y (1993) Stabilization of sugar-boronic esters of indolylboronic acid in water via sugar–indole interaction: a notable selectivity in oligosaccharides. Bull Chem Soc Jpn 66:2965–2971. https://doi.org/10.1246/bcsj.66.2965
70. Zhao Y, Sun X, Zhang G et al (2011) Interaction of mesoporous silica nanoparticles with human red blood cell membranes: size and surface effects. ACS Nano 5:1366–1375. https://doi.org/10.1021/nn103077k
71. Manivasagam VK, Popat KC (2023) Improved hemocompatibility on superhemophobic micro–nano-structured titanium surfaces. Bioengineering 10:43. https://doi.org/10.3390/bioengineering10010043
72. Manivasagam VK, Sabino RM, Kantam P, Popat KC (2021) Surface modification strategies to improve titanium hemocompatibility: a comprehensive review. Mater Adv 2:5824–5842. https://doi.org/10.1039/d1ma00367d
73. Anjaneyulu U, Swaroop VK, Vijayalakshmi U (2016) Preparation and characterization of novel Ag doped hydroxyapatite–Fe 3 O 4–chitosan hybrid composites and in vitro biological evaluations for orthopaedic applications. RSC Adv 6:10997–11007. https://doi.org/10.1039/C5RA21479C
74. Fink K, Uchman M (2021) Boron cluster compounds as new chemical leads for antimicrobial therapy. Coord Chem Rev 431:213684. https://doi.org/10.1016/j.ccr.2020.213684
75. Yilmaz MT (2012) Minimum inhibitory and minimum bactericidal concentrations of boron compounds against several bacterial strains. Turkish J Med Sci 42:1423–1429. https://doi.org/10.3906/sag-1205-83
76. Orak F, Nazik H, Yalcinkaya KT et al (2022) Antifungal efficacy of pure boron on yeast and mold isolates causing superficial mycosis. J Pak Med Assoc 72:1330–1334. https://doi.org/10.47391/JPMA.2219
77. Moore JA, Committee ES (1997) An assessment of boric acid and borax using the IEHR evaluative process for assessing human developmental and reproductive toxicity of agents. Reprod Toxicol 11:123–160. https://doi.org/10.1016/S0890-6238(96)00204-3